Available online at www.sciencedirect.com
ScienceDirect
Icarus 195 (2008) 169–183
ICARUS
www.elsevier.com/locate/icarus

Generation and performance of automated jarosite mineral detectors for visible/near-infrared spectrometers at Mars

Martha S. Gilmore [a,*], Benjamin Bornstein [b], Matthew D. Merrill [a,1], Rebecca Castaño [b], James P. Greenwood [a]

[a] *Department of Earth and Environmental Sciences, Wesleyan University, 265 Church St., Middletown, CT 06459, USA*
[b] *Jet Propulsion Laboratory, 4800 Oak Grove Drive, Pasadena, CA 91109, USA*

Received 13 June 2006; revised 31 August 2007

Available online 23 December 2007

Abstract

We have developed two automated detectors that can recognize the sulfate mineral jarosite in unknown visible to near-infrared spectra (350–2500 nm). The two detectors are optimized for use within the terrestrial and martian atmospheres. The detectors are built from Support Vector Machines trained using a generative model to create linear mixtures of library mineral spectra. Both detectors performed with an average ∼90% accuracy on laboratory spectra of single minerals and the laboratory and field spectra of rocks collected in a hydrothermal environment. This type of algorithm will contribute to the efficiency of onboard data analysis of landed and orbital visible/near-infrared spectrometers at Mars.

Keywords: Mars, surface; Spectroscopy; Instrumentation; Mineralogy

1. Introduction

Data return from planetary missions is fundamentally constrained by (1) bandwidth constraints on the downlink channel, (2) limited interaction with Earth, (3) the limited storage and computing resources on a spacecraft, and (4) finite instrument lifetime. As a consequence, more data can be collected during a mission than can be returned to Earth. These limitations require that all data are triaged on planetary missions, where highest priority data may be downlinked firstly and/or with minimal compression and lowest priority data may not be collected or returned at all. For example, the Mars Exploration Rovers (MER) collect substantially more images for navigation than can be downlinked. While compressed thumbnails may be downloaded to assess if the full image should be transmitted, a new approach to increase the mission science return is to collect more images and prioritize data onboard according to criteria determined by the science team. This has been demonstrated on the MER mission with the onboard detection of dust devils and clouds (Castaño, 2006a, 2006; Schenker, 2006; Bornstein et al., 2007). These events are typically rare, thus the number of phenomena contained in the data set for the same downlink allocation can be increased by monitoring over a greater time period and selectively transmitting data containing the features of high interest.

Future rovers at Mars that utilize a variety of remote sensing instruments over long periods of time (years) may traverse many 10s of kilometers during the mission lifetime. The science return of future robotic missions to Mars can be enhanced by automating routine processing tasks, including the recognition of high priority data within the entire collected set. In traditional terrestrial field geology and during the MER missions, interesting features that provide critical clues to the history of the surface may be found in localized patches. For example, in the Columbia Hills, the Paso Robles soil is a unique localized material interpreted due to its mineralogy to be an acidic evaporite deposit (Ming et al., 2006; Morris et al., 2006); clay minerals may be limited to rocks at Wooly Patch (Wang et al., 2006). The hydrous mineral jarosite measured at Meridiani

* Corresponding author.
E-mail address: mgilmore@wesleyan.edu (M.S. Gilmore).
[1] Currently at the Eastern Energy Resources Team, US Geological Survey, 954 National Center, Reston, VA 20192, USA.

0019-1035/$ – see front matter
doi:10.1016/j.icarus.2007.11.025

Planum (Klingelhöfer et al., 2004) is contained within meter-scale outcrops and has not yet been confirmed from orbit. The capability to identify these types of features onboard rovers, in particular during extended traverses, will ensure that significant discoveries are not overlooked. It is critical that future rovers be able to detect high priority targets such as minerals formed in the presence of water, unusual materials, or systematic changes in materials that may correspond to a geologic contact. Autonomous systems can also increase opportunistic science discoveries by collecting and analyzing data that would not otherwise be scheduled (e.g., data collection during a rover traverse), and in exploratory data analysis, where rapid feedback may enhance discovery potential (e.g., recognition of a high priority target that would alter a command sequence such as collecting more data or changing the rover path).

Spectroscopy is a primary tool for the identification of the mineralogy of Mars. Here we develop onboard intelligence sufficient to autonomously recognize geologically important minerals within spectrometer measurements of soil and rock samples, and thus to guide the selection, measurement and return of these data from Mars. In this investigation, we utilize the visible to near-infrared (VNIR, 350–2500 nm) portion of the spectrum as both the instrumentation and extensive spectral libraries are available. Iron-bearing minerals, clays, sulfates and carbonates have distinct absorptions in this region of the spectrum and have been recognized on Mars (where present) by the ISM instrument on Phobos 2 (Mustard et al., 1993; Mustard and Sunshine, 1995), the IRS instrument on Mariner 6/7 (Herr et al., 1972; Calvin et al., 1994), the OMEGA instrument on Mars Express (Bibring et al., 2005), and the CRISM instrument on the Mars Reconnaissance Orbiter (Mustard et al., 2007). The usefulness of VNIR reflectance point spectrometers for mineralogy and geologic interpretation has been demonstrated by rover field tests (Jolliff et al., 2002; Johnson et al., 2001; Gazis and Roush, 2001). The Imager for Mars Pathfinder (IMP) and Panoramic Camera (Pancam) instruments, with 15 (IMP) and 13 (Pancam) filters operating over the range ∼440–1000 nm (Smith et al., 1997; Bell et al., 2003), have classified materials based on their ferrous and ferric mineralogy at the Pathfinder and MER sites, respectively (Bell et al., 2000, 2004; Farrand et al., 2006). We anticipate that future Mars rovers will be equipped with high spectral resolution (10–100s channels) VNIR spectrometers. While the software described here is specific to high-resolution VNIR spectra over the 350–2500 nm range, the methods described here may be applied to other spectral data sets (e.g., thermal emission) if sufficient laboratory, field, and library spectra are available.

Spectral classification has been approached using a number of methodologies, including rule-based expert systems (Gazis and Roush, 2001; Clark et al., 2003), Bayes nets (Ramsey et al., 2002) and artificial neural networks (Gilmore et al., 2000; Bornstein et al., 2005). Rule-based systems such as Tetracorder (Clark et al., 2003) are capable of detecting many minerals in a single mixed spectrum, but are computationally intensive and require significant input from the user to maximize the result. To reduce computation time and increase portability, we employ an approach where we seek to identify specific mineral compositions within unknown spectra. This is accomplished by employing Support Vector Machines (SVMs), a supervised classification algorithm. Using known mineral spectra, each classifier is trained to recognize the spectral characteristics of a geologically important mineral or mineral subclass. For Mars, these are minerals associated with the presence of water. In this work, we report on the development of an algorithm to detect the sulfate mineral jarosite ($(K, Na, H_3O)Fe_3(SO_4)_2(OH)_6$) in visible–near infrared (VNIR) spectra; this hydrous mineral has been measured within outcrops on Meridiani Planum by the Mars Exploration Rover (MER) Opportunity (Klingelhöfer et al., 2004).

2. The jarosite detector

2.1. Support Vector Machines

Support Vector Machines (SVMs) are a family of classifiers that attempt to identify the optimal decision boundary that separates input data into two classes after application of a kernel function to each datum (DeCoste and Mazzoni, 2003). The decision boundary is computed empirically, where the SVM is trained on a set of positive and negative examples, in this case, VNIR spectra of minerals. The SVM output is the sum of dot products of support vectors and reflectance values adjusted by a constant. Since supervised machine learning classifiers enable minerals of interest to be targeted directly and since classifiers, by design, create an internal representation to summarize their training data (spectra), they reduce computation requirements making them suitable for onboard classification and downlink prioritization. For instance, as part of the Autonomous Sciencecraft Experiment, a SVM onboard the Earth Observing One (EO-1) spacecraft identifies transient events of the cryosphere such as the freezing and thawing of lakes (Chien et al., 2005; Castaño et al., 2006b).

A primary disadvantage of Support Vector Machines is that the time to classify points is proportional to the number of support vectors, which for complicated problems can be as large as the number of training examples. Since we wanted to train on thousands of examples, this would result in unreasonably slow classification. To minimize the computation time required to classify new spectra, we restricted the design of our detectors to linear kernel SVMs. We used a cross-validated testing approach to evaluate several elaborate and computationally expensive kernels but none showed an appreciable loss in classification accuracy compared to linear kernels.

2.2. Generative learning model

A potential drawback of many types of supervised machine learning algorithms is that large numbers of training examples are often required for the classifier to converge (learn). During the construction of our Artificial Neural Network (ANN) carbonate detector (Gilmore et al., 2000; Bornstein et al., 2005) we found that tens of spectra were insufficient to train the ANN to predict the presence or absence of mineral endmembers. This

presented a problem since collecting only a few dozen samples often requires days of fieldwork followed by petrographic or geochemical measurements to verify the modal mineralogy of each sample. While it is possible to use spectral libraries to alleviate the labor burden of sample collection and analysis, for our purposes, spectral libraries have two drawbacks: (1) they often contain ten or fewer spectra per sample and (2) the spectrum is usually measured in the laboratory, which yields data of generally pure endmember minerals that are not representative of typical rocks in the field. For an SVM detector to perform well on field-collected spectra, it must be trained on field data or data with similar variability.

In an effort to inexpensively obtain spectral data with many of the characteristics of field data, we have begun to develop a generative model for input spectra. The model starts with a database populated from two well-known spectral libraries: JPL's Advanced Spaceborne Thermal Emission and Reflection Radiometer (ASTER) library (Hooke, S., 2000. The JPL ASTER Spectral Library v1.1, http://speclib.jpl.nasa.gov) and the US Geological Survey's (USGS) Speclib04 (Clark et al., 1993). To this database we define virtual rocks, defined as containing one or more constituent minerals in specific percentages or percentage ranges constrained by terrestrial and martian petrology (Table 1; Fig. 1). Within the defined ranges, all percentages are chosen using a uniform pseudorandom number generator. For each virtual rock description, we classify constituent minerals as essential, accessory, or accidental. Essential minerals are required to occur in a rock at the percentage (or within the range of percentages) specified. Accessory minerals may occur in the virtual rock type are added to a rock if the chosen percentages for essential minerals do not sum to 100. Finally, accidental minerals that rarely occur in the virtual rock type are added to rocks with low probability (usually $<10\%$ of the rocks generated). The compositions of the virtual rocks were selected to represent rocks known (from martian meteorites and orbital spectroscopy) and predicted to occur on Mars. This includes basic volcanic rocks (i.e., basalts) and their weathering products that likely comprise the majority of the surface, as well as minerals of interest at Mars (minerals associated with water such as carbonates and evaporates; Table 2). The classification of minerals as essential, accessory, or accidental and their percentages are constrained to be geologically reasonable.

To generate spectra for each virtual rock, we take the rock's constituent mineral spectra and corresponding percentages and apply a mixing model. In this study, we applied a linear mixing model. Let $r(m, b)$ be the reflectance for endmember m at bandwidth b. Then, given the mix percentage for each endmember w_m, the mixed reflectance for band b, R_b, is:

$$R_b = \sum_m w_m r(m, b). \tag{1}$$

Table 1
Example rock classification input into the generative model

Virtual rock: Basalt			
Essential minerals		Accessory minerals	
Name	Mineral in rock (%)	Name	Mineral in rock (%)
Labradorite	40–55	Hematite	1–10
Augite	31–45	Magnetite	1–10
Olivine	0–20	Ilmenite	1–10
		Quartz	1–10

Table 2
Minerals included in the "non-jarosite" class while training the SVM detector

Class	Minerals
Martian igneous and weathering products	Augite, chromite, clinochlore, kaolinite, montmorillonite, olivine, pigeonite, siderite, talc
Minerals often associated with jarosite	Alunite, anhydrite, epsomite, ferrihydrite, goethite, gypsum, hematite, lepidocrosite, magnetite

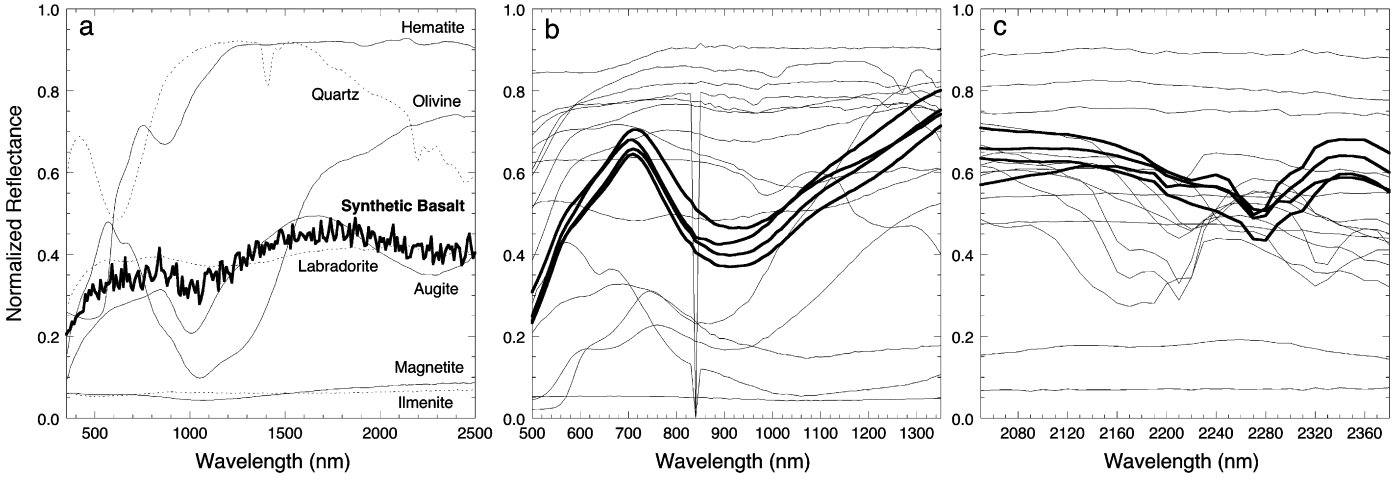

Fig. 1. Spectra produced using the generative model. (a) Example of synthetic basalt spectrum (bold) generated according to the guidelines in Table 1. The basalt spectrum comprises 47% labradorite, 37% augite, 4% each of hematite, magnetite, olivine, 3% quartz and 2% ilmenite. Gaussian noise (2%) is also added to the spectrum. Spectra of constituent endmember minerals are from the USGS Speclib04 (Clark et al., 1993): augite NMNH120049, hematite 2% + 98% Qtz GDS76, ilmentite HS231.3B, labrardorite HS105.3B, magnetite HS195.3B, olivine NMNH137044.a 160 μm, quartz HS117.3B averturine. Example synthetic rock spectra input into the generative model, (b) 500–1350 nm, (c) 2050–2380 nm. Spectra are single, double, ternary and quaternary linear mixtures of the endmembers listed in Table 2. Example training spectra that are labeled as jarosite are in bold.

Thus, under the linear mixing model, mixed reflectances are simply weighted linear combinations of endmember spectra. Recall, however, the spectra are drawn from spectral libraries, which contain predominately laboratory spectra. To simulate instrument and other noise encountered when taking field measurements, we add pseudorandom Gaussian noise with mean zero and variance σ:

$$R_b = \sum_m w_m r(m, b) + N[0, \sigma]. \quad (2)$$

While such a mixing model is simplistic, it has allowed us to create and test our generative model framework and it can provide a wealth of spectra with many subtle variations to train SVMs and other machine learning techniques. We are currently developing a set of richer, nonlinear mixing models based on the reflectance and refraction models of Hapke (1993).

2.3. Detector construction

To reduce computation time, the detector input is limited to those regions of the VNIR spectrum that contain characteristic absorption features of jarosite: a steep slope from 350–700 nm which is the edge of a charge transfer band, ferric crystal field transition bands at 430 nm and ~930 nm, and bound water vibration bands at ~1470, 1850, 2250, 2270 and 2500 nm (Hunt et al., 1971; Rossman, 1976; Hunt and Ashley, 1979; Clark et al., 1990; Morris et al., 1996; Bishop and Murad, 2005; Cloutis et al., 2006) (Fig. 2). The sharp 430 nm band present in the spectra of jarosite and several other ferric sulfates (e.g., Rossman, 1976; Cloutis et al., 2006), is lost in the noise in some of our field spectra and thus omitted in this version of the detector. Schwertmannite is unique among ferric sulfates in that is shares both the 430 and ~920 nm bands with jarosite, however, the spectra differ significantly in the near-infrared region (Bishop and Murad, 1996). Ferric oxides such as goethite and hematite and ferrous minerals such as olivine exhibit absorptions in the 800–1000 nm range, but are distinguishable from jarosite in the near infrared, likewise some layer silicates (e.g., chlorite, muscovite) and carbonates (e.g., calcite) have absorptions ~2270 nm but are distinct from jarosite in the visible (Hunt and Salisbury, 1970; Gaffey, 1987). Nontronite exhibits bands at ~450, ~900 and ~2290 nm which are similar to jarosite and may cause confusion between the two minerals, however nontronite has additional bands at ~640, ~1420, ~1900 and ~2200 nm that are lacking in the jarosite spectrum (Sherman and Vergo, 1988; Clark et al., 1990; Bishop et al., 2002). We sought to avoid noise in the spectra due to atmospheric water vapor at 1400 and 1900 nm that would be encountered during field tests. Based on these constraints, we selected two spectral intervals over which the detector operates: 500–1350 and 2050–2380 nm. Compositional variability in jarosite (natrojarosite $NaFe_3(SO_4)_2(OH)_6$, plumbojarosite $PbFe_3(SO_4)_4(OH)_{12}$, hydronium jarosite $(H_3O)Fe_3(SO_4)_2(OH)_6$) are found to have minimal differences (<~30 nm) on the position of the ~930 nm band minimum (Krenn et al., 2001; Bishop and Murad, 2005; Cloutis et al., 2006), and thus the detector should apply to these endmembers and their solid solutions.

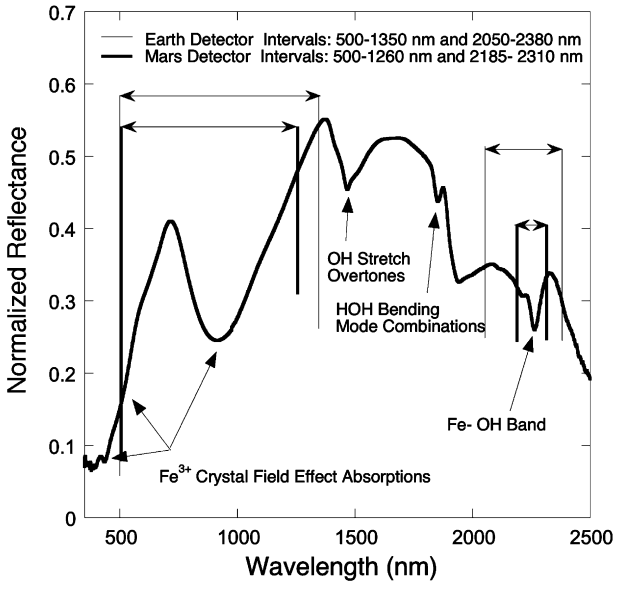

Fig. 2. Input intervals for the SVM jarosite detectors as well as jarosite band assignments and locations. Laboratory spectrum of jarosite collected at Sulfur Springs.

The generative model was used to create linear mixtures of spectral library data for SVM training (Fig. 1). Nine different jarosite spectra representing the K, Na and H_3O varieties of the mineral from the United States Geologic Survey (USGS) Speclib04 database were introduced to the detector for training purposes. Training spectra for the non-jarosite class includes minerals that are often found in the presence of jarosite (Table 2). In total 100 spectra were created to train the SVM. Of these, 54 were jarosites and 46 were non-jarosite with the latter group comprised of equal amounts of pure endmember, binary, tertiary and quaternary linear mixtures included in percentages defined by the generative model. All library spectra were smoothed to a spectral resolution of 10 nm to ensure a consistent training set.

Upon completion of the original detector, an additional detector was created with inputs tailored to avoid spectral absorptions expected in the martian atmosphere. The atmosphere of Mars contains 95% CO_2, 0.13% O_2, 0.07% CO and 0.03% H_2O (Owen, 1992), resulting in characteristic absorptions in the VNIR (Owen, 1992; Bell et al., 1994). The presence of CO_2 bands at 2052, 2114 and 2150 nm, CO bands at 2331 and 2357 nm and an H_2O band at 1330 nm limits the input ranges of the Mars-based detector to 500–1260 and 2185–2310 nm (Fig. 2). Separate empirically-derived classification boundaries for the Mars-based and Earth-based detectors result in two different ranges of output values.

2.4. Detector testing

After training, the detector was tested on laboratory and field spectra of a variety of natural samples of rocks and minerals (Table 3, Figs. 3–5). Spectra were collected with an ASD FieldSpec® FR operating over a total range of 350–2500 nm.

Table 3
Minerals used for jarosite detector testing. A detector output > zero corresponds to a positive identification of jarosite. Incorrect detections are indicated in boldface type

Sample		Dominant minerals, mode where determined				Band depth		Detector score		Notes
		Catalog/ hand sample	Vis/NIR	XRD	SEM/EDS	923 nm	2267 nm	Earth	Mars	
Peoples Museum (catalog #)										
1.	Biotite	100% Bi	Bi			0.25	0.16	−1.53	−1.80	Crystalline
2.	Clinochlore (#4134)	100% Cl	Cl			0.15	0.24	−1.43	−1.45	Crystalline; West Chester, PA
3.	Kaolinite 1	100% Ka	Ka			0.01	0.01	−2.89	−4.09	Crystalline
4.	Kaolinite 2	Ka	Ka			0.01	0.21	−1.55	−1.79	
5.	Muscovite	100% Mu	Mu			0.08	0.01	−1.39	−1.73	Crystalline
6.	Phlogopite	100% Phl	Phl?			0.18	0.15	−0.99	−1.48	Crystalline
7.	Talc	100% Ta	Ta			0.19	0.22	−2.11	−1.63	Crystalline
8.	Montmorillonite		Mo			0.05	0.00	−2.31	−2.72	
9.	Nontronite (#14138)	No	No			0.15	0.10	−0.42	**0.20**	Crystalline and massive; Conklin Quarry, Lincoln, RI
10.	Gypsum	100% Gy	Gy			0.06	0.09	−0.07	−0.19	Crystalline
11.	Halite (#11442)	100% Ha	Ha			0.01	0.01	−2.49	−3.36	Single crystal; Detroit, MI
12.	Sylvite	100% Sy	No library spectrum			0.02	0.01	−0.45	**0.02**	
13.	Alunite (#4358)	100% Al	Al			0.00	0.00	−1.01	−2.64	Crystalline; Muzay, Hungary
14.	Jarosite (#12300)	Ja	Ja	Ja		0.52	0.38	0.94	0.60	Crystalline and coatings; Swansea Mine, Tintic Utah
15.	Barite (#8308)	100% Ba	Npi			0.00	0.01	−1.87	−2.63	Crystalline; Cheshire, CT
16.	Magnesite (#2154)	100% Ma	Ma			0.00	0.10	−1.76	−3.09	Crystalline
17.	Siderite 1 (#4466)	Si	Si?			0.10	0.01	−1.36	−1.97	Crystalline
18.	Siderite 2 (#8668)	Si	Si?			0.08	0.03	−1.47	−1.74	Crystalline
19.	Hematite 1 (#22)	He	He			0.27	0.03	−1.66	−2.14	Red
20.	Hematite 2	100% He	He			0.35	0.03	−1.63	−1.52	Semi-specular
31.	Goethite (#13935)	100% Go	Go			0.25	0.03	−1.13	−1.31	Crystalline
22.	Sulfur	100% Su	Su			0.00	0.03	−2.64	−4.27	Crystalline
23.	jm1	Ja, Ba	Ja	Ja		0.53	0.43	1.20	0.89	
24.	jm2	Ja, Ba	Ja	Ja		0.54	0.40	0.62	0.15	
25.	jj1	Ja	Ja			0.70	0.59	2.35	2.25	
26.	jj2	Ja	Ja			0.68	0.58	0.50	0.00	
27.	jj3	Ja	Ja			0.57	0.46	0.35	**−0.05**	
27.	jj4	Ja	Ja			0.55	0.44	1.25	1.11	
29.	jj5	Ja	Ja			0.52	0.43	0.84	0.59	
30.	Barite	Ba	Npi			0.01	0.01	−1.55	−2.00	
St. Lucia samples, spectra collected in lab										
31.	CH2b		Phy			0.00	0.04	−1.84	−3.00	
32.	White vein rock		Al, Gy?			0.00	0.01	−1.14	−2.99	
33.	IMT-1		Ja, Al, Phy	Al, Qu		0.15	0.06	**−0.91**	**−1.34**	
34.	IMT-1or		Ja, Al, Gy	Ja, Al, Gy, Qu	28% Ja, Al, Gy	0.40	0.15	1.04	1.67	
35.	IMT-2		Ka, Py, No?			0.07	0.00	−1.85	−2.33	
36.	IMT-3a		Ka			0.01	0.03	−0.60	−1.54	
37.	IMT-3b		Ja, Go, Al		Ja, FeOx, S, Qu	0.25	0.11	0.11	0.30	
38.	CH1		Go, Ja, Al	Go, Qu	Al, Ja, S, FeOx, Qu	0.37	0.07	0.15	0.52	
39.	CH3		Phy?			0.00	0.01	−0.83	−1.82	
40.	CH4		Phy?			0.00	0.01	−0.57	−1.87	
41.	CH5		Phy, S, Al?	Qu		0.00	0.05	−0.07	−1.39	
42.	CH6		Go		Su, Pyr, Org	0.40	0.01	−0.68	−0.44	

(*continued on next page*)

Table 3 (*continued*)

Sample		Dominant minerals, mode where determined				Band depth		Detector score		Notes
		Catalog/ hand sample	Vis/NIR	XRD	SEM/EDS	923 nm	2267 nm	Earth	Mars	
43.	CH6w		Al	Qu, Su		0.03	0.02	−1.02	−2.30	
44.	M1		Py, Ka?			0.15	0.03	−1.27	−1.69	Dacite
45.	M3		Py, Ka?			0.13	0.01	−1.09	−1.47	Dacite
46.	b/t hottest pools		Phy			0.01	0.04	−1.48	−2.49	
47.	Ex-wall GC		Phy			0.01	0.00	−1.23	−3.30	
48.	Ex-wall GCg		Al			0.09	0.04	−2.06	−2.70	
49.	In situ rock No. SP-1		Al, Phy			0.08	0.05	−1.07	−1.47	
50.	In situ rock No. SP-1w		Al, Phy			0.01	0.07	**1.87**	**1.24**	
51.	Jarosite rock[d]		Go, Al	Go, Qu	FeOx, Qu	0.39	0.01	−0.91	−0.64	
52.	S13Y		Ja, Al,		Al, Qu, 20% Ja, Gy, Ru	0.44	0.08	0.96	2.52	
53.	S13W		Al	Qu, Al, Ja?		0.00	0.00	−1.66	−2.85	
54.	S13WY		Al			0.04	0.00	−0.28	−0.53	
55.	S1		Al, Phy			0.01	0.04	−1.17	−1.76	
56.	S2W		Phy, Al?			0.00	0.03	−1.76	−3.08	
57.	S2O		Ja, Al			0.46	0.21	1.56	2.41	
58.	S2Y		Ja, Al			0.12	0.07	**−0.19**	**−0.92**	
59.	S3P		Phy			0.00	0.10	**0.24**	−0.62	Dacite
60.	S3O		Ja. Phy			0.46	0.24	1.16	1.84	
61.	S3G		Py, Phy			0.05	0.02	−1.65	−2.19	
62.	S4O	Gy	Ja, Gy, Al	Al, Ja	49% Ja, Al, Gy, Qu	0.50	0.20	0.71	1.22	
63.	S4W	Gy	Gy, Al, Phy	Qu, Phy		0.00	0.00	−1.57	−2.09	
64.	S4bO	Gy	Ja, Gy, Al			0.56	0.23	0.94	1.90	
65.	S4xtals	Gy	Gy			0.06	0.13	−0.45	−0.53	Single crystals
66.	S6P	Qu	?			0.00	0.03	−0.53	−1.61	
67.	S6O	Qu	Ja, Al			0.35	0.02	1.35	2.98	
68.	S7		Mo			0.04	0.00	−1.85	−2.43	
69.	S8B	Su	Su, Phy			0.01	0.01	−1.27	−1.70	
70.	S8Y	Su	Su			0.02	0.00	−0.78	−1.46	
71.	S9O		Go, Phy		FeOx, Si	0.57	0.00	−0.87	−0.24	
72.	S9(2)O		Go, Phy		FeOx, Si	0.55	0.00	−0.58	**0.67**	
73.	S10OT		Ja, Phy	Qu, Go, Ja, Al	FeOx, Ja?, S, Qu	0.32	0.06	0.26	0.62	
74.	S10O		Go, Phy			0.40	0.01	−0.06	**0.58**	
75.	S11GrY		Ja, Al, Phy	Ja, Al, Qu		0.26	0.18	0.35	0.27	Dacite
76.	S11Y		Ja			0.35	0.26	0.91	0.81	
77.	S11BG		Phy			0.01	0.00	−1.63	−2.24	
78.	S12P		Gy	Gy, Qu	Gy, Al, Qu	0.00	0.05	**0.99**	**0.72**	
79.	S12PW		Phy			0.00	0.00	−0.01	−0.28	
80.	ST-HEM1		Phy			0.02	0.00	−1.02	−1.18	
81.	ST-HEM3		Phy			0.01	0.00	−0.53	−0.57	
82.	ST-HEM4		Phy			0.01	0.02	−0.77	−1.35	
83.	ST-HEM5		Phy			0.01	0.01	−0.64	−0.77	
84.	ST-7aOC-Y		Ja, Al	Ja, Al, Gy	31% Ja, Al, Qu, Fel	0.55	0.25	1.92	3.21	
85.	ST7aOC-W		Al			0.03	0.01	−1.11	−1.81	
86.	ST-D-D		Phy			0.05	0.02	−1.12	−1.59	
87.	ST-D-Y		Ka			0.00	0.00	−1.26	−2.82	
88.	ST-D-W		Ka			0.00	0.00	−1.60	−3.02	
89.	ST7aDP-DP		Al, Phy			0.02	0.03	−1.49	−3.04	
90.	ST7aDP-Y		Al, Su			0.00	0.00	−1.20	−3.00	
91.	ST7aDP-W		Al			0.00	0.00	−2.30	−4.02	
92.	WCGR-W		Phy			0.00	0.07	−0.81	−2.78	
93.	ST7aLP-P		Phy			0.00	0.03	−2.86	−4.54	
94.	ST7aLP-Gr	Algae	Org, Phy			0.00	0.03	−0.89	−3.66	
95.	St71LP-W		Org, Phy			0.01	0.02	−2.34	−2.95	
96.	OWR-D		Go, Ka			0.50	0.00	−1.02	−0.76	
97.	OWR-W		Ka			0.04	0.00	−1.16	−1.33	
98.	OWR-O		Go, Ka			0.09	0.00	**0.05**	**0.89**	
99.	DC-P		Go, Phy			0.09	0.05	−1.22	−1.83	

Table 3 (*continued*)

Sample		Dominant minerals, mode where determined				Band depth		Detector score		Notes
		Catalog/ hand sample	Vis/NIR	XRD	SEM/EDS	923 nm	2267 nm	Earth	Mars	
100.	DC-Pk		Phy			0.02	0.07	**0.10**	−0.47	
St. Lucia samples, XRD powders										
101.	GCorPre-powder		Ja, Ka	Ja, Al, Qu, Ka	19% Ja, Pyr, Qu	0.31	0.14	**−0.05**	0.45	
102.	ST7a-or-x		Ja, Al	Ja, Al, Gy?	Ja, Al, Qu, Fel	0.34	0.16	1.30	1.57	
103.	S11or-x		Ja, Al	Ja, Al, Qu		0.28	0.17	0.76	0.47	
104.	S4or-x		Ja, Al Al, Ja, Qu, Gy	Al, Ja,	49% Ja, Al, Gy, Qu	0.39	0.17	1.24	1.53	
105.	S4yell-x		Ja, Al, Gy			0.13	0.05	**−1.63**	**−2.54**	
106.	S4white-x		Ka	Qu, Phy		0.00	0.00	−2.79	−4.31	
107.	S12pink-x		Gy	Gy, Qu	Gy, Al	0.00	0.03	−0.75	−2.20	
108.	S13white-x		Al	Qu, Al, Ja?	Al, Qu, Ja, Gy	0.00	0.00	−3.05	−5.21	
109.	S10		Go	Qu, Go, Ja, Al	FeOx, Ja, S, Qu	0.45	0.01	−0.51	−0.36	
110.	GCor-x		Ja, Ka	Ja, Al, Qu, Ka	19% Ja, Pyr, Qu	0.14	0.05	**−0.91**	**−1.50**	
St. Lucia field targets[a]										
111.	Drk green precip	Algae	Org			0.01	0.01	−0.34	−1.84	
112.	Yell precip		Ja			0.41	0.19	1.25	2.41	
113.	White earthy precip		Al			0.01	0.01	−1.01	−1.55	
114.	More white stuff		Al			0.00	0.01	−1.10	−1.59	
115.	Pale earthy red-brown		Al, Gy			0.07	0.02	−1.02	−1.43	
116.	Pale greyish green		Gy. Su			0.13	0.01	−1.59	−1.73	
117.	Sulfur	Su	Su			0.03	0.01	−2.56	−4.36	
118.	SulfurT	Su	Su			0.09	0.00	−2.17	−2.92	
119.	CH1		Ja, Go	Go, Qu	FeOx, Su, Al, Ja, Qu	0.46	0.07	−0.65	−0.20	
120.	Yell rx small stream	Algae	Org			0.13	0.08	−0.48	−0.42	
121.	CH2b		Org			0.01	0.07	−0.67	−0.93	
122.	CH6		Go			0.52	0.02	−0.56	**0.14**	
123.	CH3	Algae, Su	Org, Su, Phy			0.01	0.02	−1.19	−1.67	
124.	CH4	Algae, Su	Org, Su, Phy			0.00	0.01	−0.95	−1.29	
125.	Brown algal mat	Algae	Org			0.00	0.02	−0.32	−1.30	
126.	White filamentous goo		Org			0.03	0.01	−1.29	−1.34	
127.	Orange goo		Org			0.21	0.15	**1.33**	**2.00**	
128.	Green goo		Org			0.00	0.04	−0.10	−1.63	
129.	Orange on rx adjacent		Go			0.31	0.02	−0.96	−1.17	
130.	Orange on rx closer		Go			0.63	0.05	−0.82	−0.73	
131.	CH5	Algae	Org, Phy	Qu		0.01	0.05	−0.65	−1.09	
132.	IMT-3a		Ja			0.23	0.11	**−0.26**	0.65	
133.	Paprika (not CH6)		Go			0.58	0.01	−0.59	**0.02**	
134.	White & black		Su, Org			0.01	0.01	−1.62	−1.60	
135.	Brown on rock		FeOx			0.09	0.02	−0.86	−0.93	
136.	Green algal		Org			0.10	0.01	**0.23**	−0.80	
137.	IMT-4		Phy			0.05	0.00	−1.29	−1.38	
138.	Paprika seep		Go			0.54	0.04	−0.82	−0.73	
139.	IMT-3b		Ja, Go		Ja, FeOx, Su	0.42	0.03	0.14	1.02	
140.	IMT-2		Go, Ka		Qu	0.15	0.01	−0.61	−0.66	
141.	White outcrop		Org			0.09	0.03	−0.69	−0.89	
142.	Orange white green		Ja, Al, Org			0.38	0.10	**−0.07**	0.32	
143.	Or crud rock		Ja, Al			0.60	0.15	1.83	3.47	
144.	IMT-1		Org			0.04	0.03	−0.32	−0.61	
Field traverses[b]										
145.	Traverse 1		Ja, Gy			0.55	0.22	0.97	2.13	
146.	Traverse 2		Gy			0.00	0.01	**0.27**	**0.19**	
147.	Traverse 3		Npi			0.01	0.02	−2.53	−2.49	

(*continued on next page*)

Table 3 (*continued*)

Sample		Dominant minerals, mode where determined			Band depth		Detector score		Notes
		Catalog/ hand sample	Vis/NIR	XRD	SEM/EDS	923 nm	2267 nm	Earth	Mars	
148.	Traverse 4		Go			0.46	0.03	−0.30	−0.19	
149.	Traverse 5		Ja			0.20	0.10	**−0.06**	0.25	
150.	Traverse 6		Npi			0.06	0.05	−1.29	−1.81	
151.	Traverse 7		Npi			0.07	0.01	−1.12	−1.49	
152.	Traverse 8		Org			0.03	0.01	**0.30**	−0.62	
153.	Traverse 9		Ja			0.42	0.07	**−0.10**	0.46	
154.	Traverse 10		Go			0.44	0.01	−0.37	−0.21	
155.	Traverse 11		Su			0.01	0.01	−1.18	−1.52	
156.	Traverse 12		Ja			0.58	0.22	1.27	2.68	
157.	Traverse 13		Org?			0.00	0.01	**1.02**	**0.94**	
158.	Traverse 15		Org?			0.00	0.01	−0.19	−0.04	
159.	Traverse 16		Ja			0.42	0.07	0.69	2.22	
160.	Traverse 17		Al			0.01	0.00	−0.69	−1.45	
161.	Traverse 18		Py?			0.13	0.02	−1.04	−1.19	
162.	Traverse 19		Npi			0.07	0.00	−1.44	−2.32	
Field spectra variable (distance) from target[c]										
163.	Incremental 4a (6.9 m)		Ja, Al			0.49	0.17	0.91	2.50	
164.	Incremental 4b (5.3 m)		Ja, Al			0.30	0.11	0.78	2.01	
165.	Incremental 4c (2.9 m)		Ja, Al			0.41	0.12	0.41	2.51	
166.	Incremental 4d (0.7 m)		Ja, Al			0.49	0.15	0.70	1.55	
167.	Incremental 5a (6.3 m)		Ja			0.34	0.05	0.53	1.74	
168.	Incremental 5b (3.7 m)		Go?			0.33	0.03	−0.28	−0.01	
169.	Incremental 5c (2.6 m)		Go?			0.63	0.03	−0.15	**0.26**	
170.	Incremental 5d (0.7 m)		Go?			0.61	0.05	−0.47	−0.16	
171.	Incremental 8a (8.5 m)		Ja, Al			0.38	0.12	0.61	1.46	
172.	Incremental 8b (5.9 m)		Ja, Al			0.22	0.09	1.28	1.96	
173.	Incremental 8c (3.1 m)		Ja, Al			0.45	0.16	1.32	3.33	
174.	Incremental 8d (0.6 m)		Ja, Al			0.48	0.15	0.82	1.86	
Field panorama[d]										
175.	Pan 1a		Gy			0.01	0.15	−1.45	−2.56	
176.	Pan 2a		Npi			0.05	0.14	−0.82	−1.37	
177.	Pan 3a		Npi			0.00	0.12	−0.54	−1.44	
178.	Pan 4a		Ja, Gy			0.57	0.14	1.37	3.45	
179.	Pan 5a		Go			0.35	0.06	−0.05	**0.82**	
180.	Pan 7a		Org?			0.12	0.00	−0.49	−0.85	
181.	Pan 8a		Ja			0.26	0.02	1.63	3.78	
JSC Mars-1 samples										
182.	Sieved to <44 μm					0.01	0.02	**0.35**	−0.02	
183.	Sieved to <44 μm					0.00	0.02	−0.05	−0.62	
184.	Sieved to 44–125 μm					0.03	0.02	**0.20**	−0.11	
185.	Sieved to 125–500 μm					0.03	0.02	−0.04	−0.27	

Mineral abbreviations: Al: alunite; Ba: barite; Bi; biotite; Cl: clinoclore; FeOx: iron oxide; Fel: feldspar; Go: goethite; Gy: gypsum; Ha: halite; He: hematite; Il: Illite; Ja: jarosite; Ka: kaolinite; Ma: magnesite; Mo: montmorillinite; Mu: muscovite; Org: organic material; No: nontronite; Npi: no positive mineral identification; Phl: phlogopite; Phy: unknown phyllosilicate; Py: pyroxene; Pyr: pyrite; Qu: quartz; Ru: rutile; Si: siderite; Su: sulfur; Sy: sylvite; Ta: talc.

[a] Spectra collected with 25° FOV bare fiber within ⩽30 cm of target.

[b] Traverse refers to spectra collected with 25° FOV bare fiber along a 50 m long traverse to simulate a Mars rover data collection strategy. Spectra were collected ⩽1 m from target.

[c] Spectra collected at variable distance from single numbered target using 1° FOV foreoptic.

[d] Spectra collected from single vantage point using 1° FOV foreoptic. Azimuths range from ∼0–60°.

Laboratory spectra of museum samples were collected at an emission angle of 20° using a 1 m fiber optic sensor with a 1° field of view transmissive foreoptic the exit end of which was ∼20 cm from the target. The spot size was determined empirically to be 12.5 cm^2. Smaller targets on collected samples were acquired using the 25° FOV bare fiber at a distance ⩽10 cm. Two 500 W tungsten quartz halogen light sources (incidence angle = 45°) were located 180° from each other 50 cm from the target; data were collected at 2 azimuths 180° apart. The instrument was optimized prior to collection of each set of spectra (10 spectra at each azimuth) and 10 scans were averaged to comprise each spectrum. Field spectra were collected using the same instrument using both the foreoptic and the bare fiber optic cable. Spectra were collected at a variety of distances and azimuths (angle between sensor and surface normal) ranging from ∼10 cm to ∼13 m and ∼0° to 60°, respectively. The instrument

was optimized at ∼5 min intervals and in response to changing light conditions. Five–ten spectra were collected of each target and each spectrum was an average of 10 scans. All absolute reflectance data were normalized to a white Spectralon® (sintered Halon) standard. Reflectance offsets between the instrument's three detectors were corrected by scaling to the middle detector region (1001–1800 nm). All spectra were averaged for each experiment and analyzed by the jarosite detectors.

Three sets of spectra were created to test the detector. Laboratory spectra were collected of 3 jarosite and 22 non-jarosite (evaporites and iron oxides) samples from Wesleyan University's Peoples Museum (Table 3). Spectra were taken of multiple locations on some samples to include variations in crystal size, habit and color. To better assess the sensitivity of the jarosite detector to mineral assemblages more typical of what is seen on a planetary surface, spectra were collected of samples taken from the Sulfur Springs hydrothermal field in St. Lucia in June and November 2004, where jarosite typically occurs as a hydrothermal alteration product (Greenwood et al., 2005, 2006). Jarosite in Sulfur Springs is characterized by a straw yellow to rusty orange color and is found as coatings on and veins within altered dacitic pyroclastic materials. Spectra of Sulfur Springs samples were taken directly in the field and laboratory spectra were collected of returned samples.

All reflectance spectra were inspected and compared to published mineral spectra to confirm both the presence or absence of jarosite and primary mineralogy (Hunt et al., 1971; Hunt and Ashley, 1979; Bishop and Murad, 2005). A spectrum of yellow-orange material that contained both a broad 923 nm absorption and 650 nm shoulder and either a sharp 423 nm absorption or a 2267 nm absorption was considered jarosite. Jarosite was confirmed in a subset of the Sulfur Springs samples by X-Ray Diffraction (XRD) and Scanning Electron Microscope Energy Dispersive Spectroscopy (SEM-EDS).

3. Results

Jarosite detector performance is indicated in Tables 3–5. Both detectors performed similarly overall and correctly classified 76–100% of the 3 classes of spectra ($n = 185$), with an average performance of 89% for the Earth-optimized and 90% for the Mars-optimized detectors. The classifiers performed comparably on the spectra of rock samples collected under both laboratory and field conditions, although the detector recognized jarosite in the field spectra better than in the spectra of rock samples measured under laboratory conditions. This may be due to the fact that many of the rocks measured in the field were selected based on the presence or absence of jarosite determined visually and thus samples with small amounts of jarosite may have been underrepresented in the field observations.

To further examine detector performance, we compare the detector output to the strength of the primary absorptions of jarosite at 923 nm and 2267 nm (Figs. 2–5). Band depths (BD = 1 − (reflectance at band center/reflectance of continuum at band center)), where the continuum is a line that fits each edge of the band (Clark and Roush, 1984) were calculated at 923 nm and 2267 nm and summed and are presented

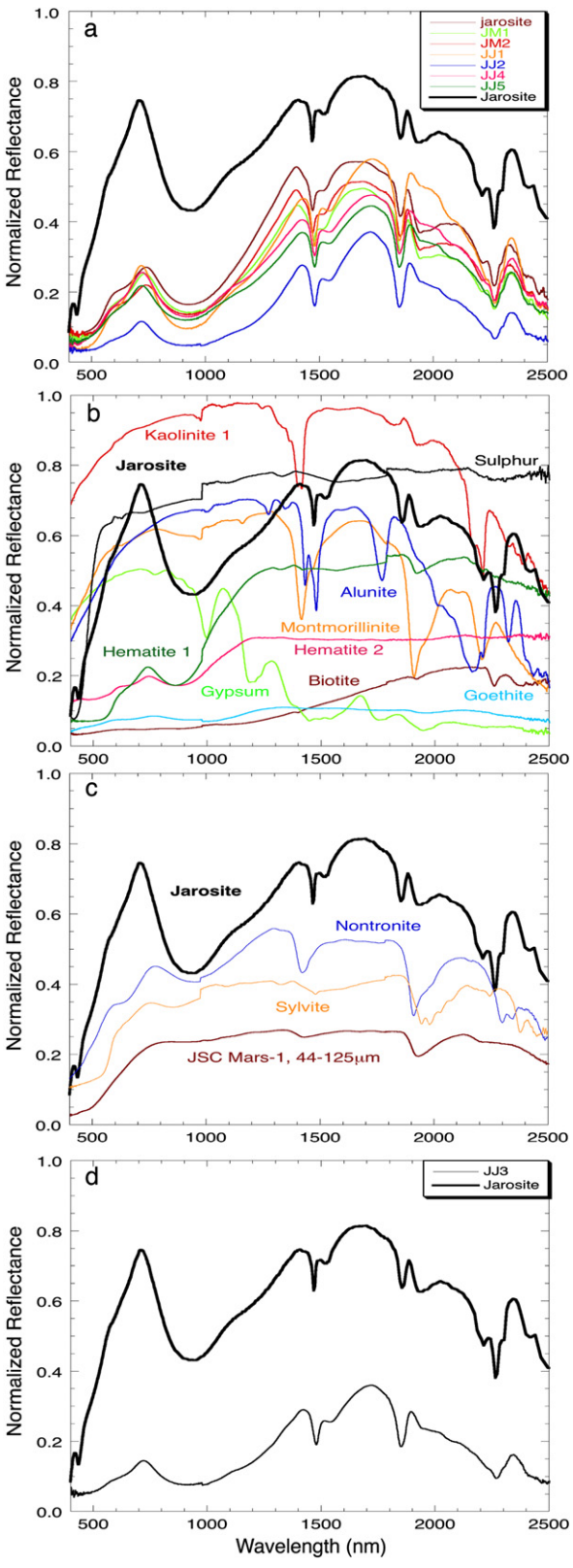

Fig. 3. Selected spectra of samples from Wesleyan's Peoples Museum. Sample descriptions can be found in Table 3. Samples are grouped according to performance of at least one of the two SVM-based mineral detectors: (a) true positives, (b) true negatives, (c) false positives, (d) false negatives. A reference jarosite spectrum (bold) is sample GDS99 k-y 200c from the USGS Speclib04 (Clark et al., 1993) and is identical in each frame.

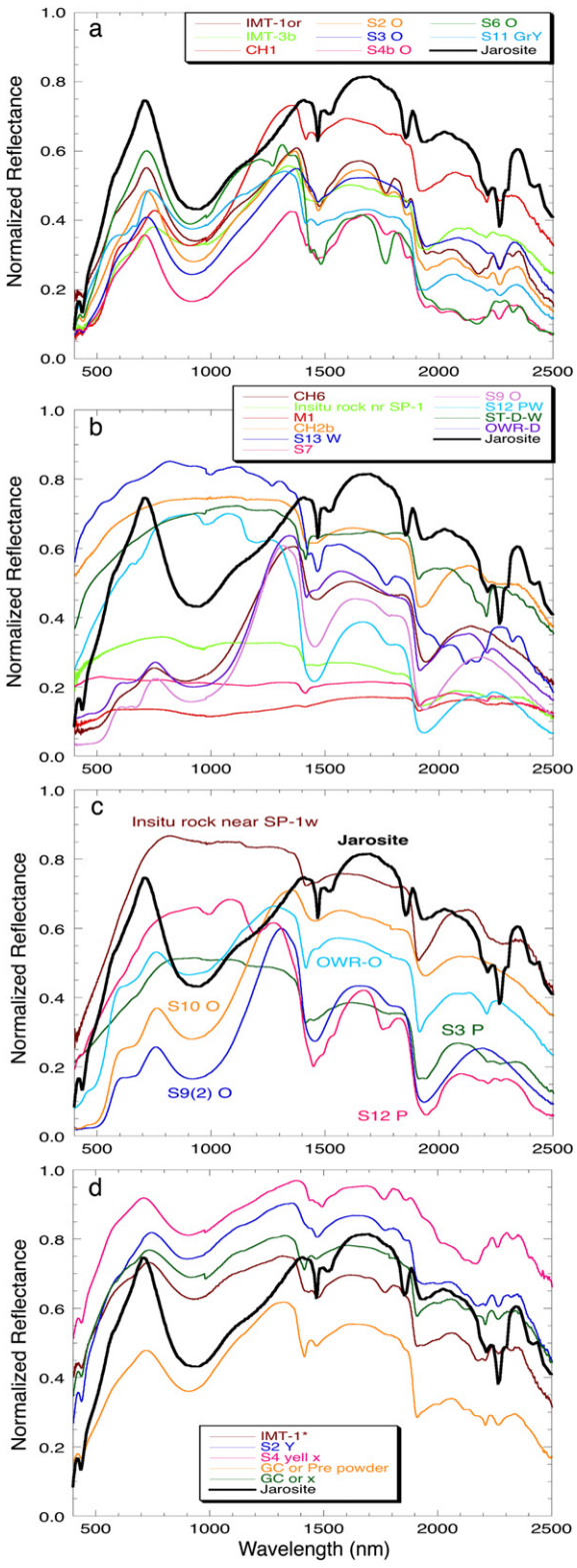

Fig. 4. Selected laboratory spectra of St. Lucia samples. Sample descriptions can be found in Table 3. Samples are grouped according to performance of at least one of the two SVM-based mineral detectors: (a) true positives, (b) true negatives, (c) false positives, (d) false negatives. A reference jarosite spectrum (bold) is sample GDS99 k-y 200c from the USGS Speclib04 (Clark et al., 1993) and is identical in each frame.

in Fig. 6 and Tables 3 and 5. Band depths are a standard metric by which spectroscopists derive mineralogy from planetary spectra. For the spectra correctly identified as jarosite (true positives) there is a significant positive correlation between the value of the sum of the jarosite absorptions and the detector output (Fig. 6a). Both detectors are sensitive to the strength of the 923 nm absorption, where all correct identifications of jarosite correspond to BD (923) $\geqslant$20%, with an average BD (923) of 43–44%. The true positive spectra have the highest average absorptions at 2267 nm with an average BD (2267) of 19–20%. Spectra correctly classified as non-jarosite (true negatives) have low average values for band depths (<15%). Thus it appears that the detector performance is dependent on the presence and strength of both primary jarosite absorptions in the input range.

A population of the spectra correctly identified as non-jarosite have BD (923) values >20%. The majority (66%) of these true negatives are the mineral goethite (FeOOH), whose spectrum has a primary absorption at ~900 nm due to Fe^{3+} crystal field transitions, but no absorption (<5%) at 2267 nm (Hunt and Ashley, 1979; Table 3; Figs. 3b, 4b, 5b). Other mineral samples correctly rejected by the detector include those with BD (923) >15% and BD (2267) >10% (biotite ($K(Fe, Mg)_3AlSi_3O_{10}(F, OH)_2$), nontronite ($Na_{0.3}Fe_2(Si,Al)_4O_{10}(OH)_2{\cdot}n(H_2O)$), phlogopite ($KMg_3(Si_3Al)O_{10}(F,OH)_2$), talc ($Mg_3Si_4O_{10}(OH)_2$), clinochlore ($(Mg, Fe)_5Al(Si_3Al)O_{10}(OH)_8$)), BD (923) >25% (hematite (Fe_2O_3)), and BD (2267) >20% (kaolinite ($Al_2Si_2O_5(OH)_4$)). The detector may be able to distinguish these minerals from jarosite by differences in the total shape of the spectra over the entire detector input interval, which is affected by chemistry and grain size of the individual specimens.

The spectra misclassified by the algorithm as jarosite (false positives, 6–7% of the validation set) generally tend to exhibit a large absorption at ~900 nm or a steep positive slope from ~500–800 nm (Figs. 3c, 4c, 5c). Minerals that were misclassified as jarosite include nontronite, goethite and sylvite (KCl), each of which exhibit both of these spectral characteristics. Three samples containing chlorophyll were also misclassified by the detectors, likely due to a steep positive slope in the 500–800 nm region. The Mars atmosphere-based detector ($n = 8$) was more likely than the Earth atmosphere-based detector ($n = 1$) to assign false positives to goethite and nontronite spectra.

Four samples of the Mars regolith simulant JSC Mars-1 (Allen et al., 1998) dry sieved to three grain sizes (2 samples at <44 μm, 1 sample each at 44–125 μm, 125–500 μm) were evaluated by both detectors. The Mars-tuned detector correctly identified all samples as non-jarosite, while the Earth-tuned detector correctly identified 50% of the samples.

False negative assignment errors comprise ~3% of the validation set (Figs. 3d, 4d, 5d). The average strength of the primary jarosite absorptions in these spectra was ~50% of that of the spectra correctly identified as jarosite (Tables 3, 5; Fig. 6). Some of these spectra are noisy and/or have low overall reflectance, which may act to reduce the strength of characteristic jarosite absorptions and result in a misassignment by the de-

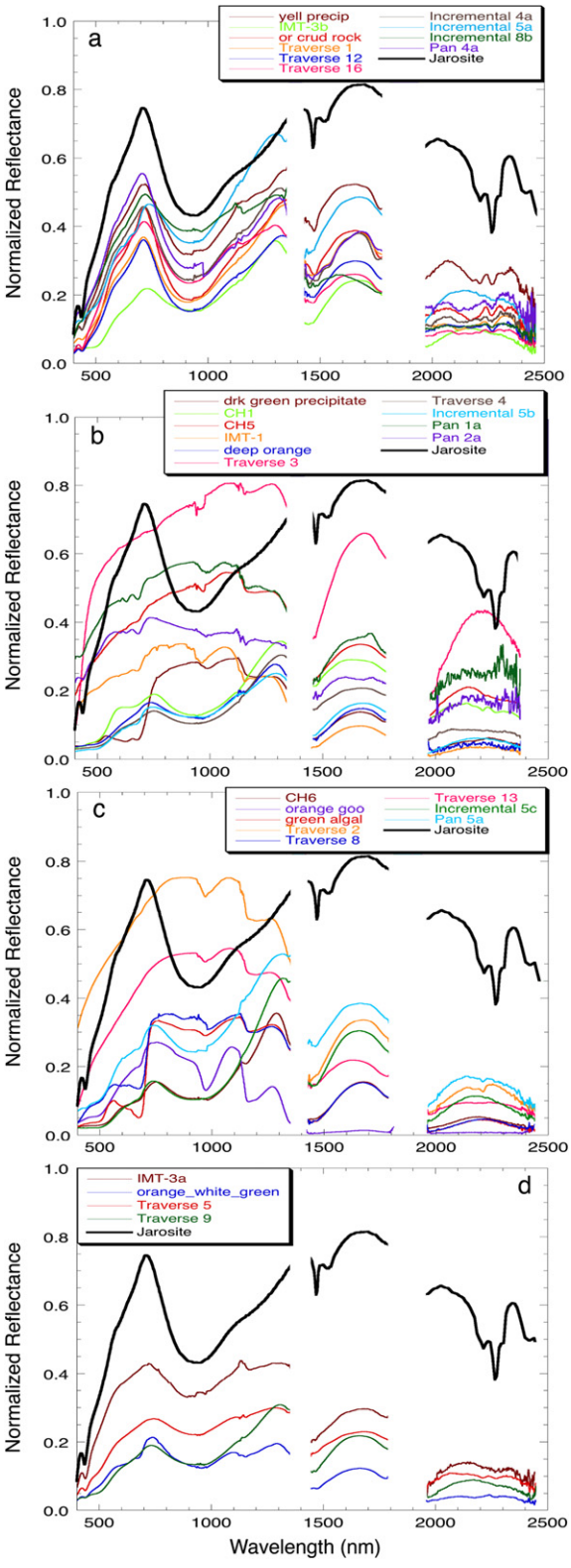

Fig. 5. Selected field spectra of St. Lucia samples. Noisy sections of the spectra due to the atmosphere are removed for clarity. Sample descriptions can be found in Table 3. Samples are grouped according to performance of at least one of the two SVM-based mineral detectors: (a) true positives, (b) true negatives, (c) false positives, (d) false negatives. A reference jarosite spectrum (bold) is sample GDS99 k-y 200c from the USGS Speclib04 (Clark et al., 1993) and is identical in each frame.

tector. Small quantities of jarosite resulting in weak bands in a mixed spectrum might also be overlooked by the detector.

The jarosite detector is a linear kernel SVM with nine support vector spectra. We applied common algebraic simplifications to reduce jarosite determination from nine detector dot products to a single dot product. Since the two detector input intervals yield 120 reflectance values, the algorithms perform only 120 floating-point multiplications, 1 subtraction and a comparison to zero per detection. On current radiation hardened processors (e.g., the MER RAD6000 operating at a maximum of 35 MIPS) a single jarosite determination would take less than a millisecond. Our detectors are available to the collaborative rover research communities spread across the Jet Propulsion Laboratory (JPL), NASA Ames, Carnegie Mellon University, the University of Minnesota, the University of Washington, the University of Michigan, the Massachusetts Institute of Technology via the Coupled Layer Architecture for Robotic Autonomy (CLARAty) (Nesnas et al., 2003) software architecture. The detector is integrated into CLARAty as a Level 2 Decision Layer component.

4. Discussion and conclusion

The SVM jarosite detector recognizes jarosite in VNIR reflectance spectra of natural mixtures under both laboratory and field conditions with an average success rate of 89–90%. The detector performance corresponds generally to the strength of the jarosite absorptions at 923 and 2267 nm as measured by band depths, where all positive detections had BD (923) >20% (average = 43%) and BD (2267) >0 (average = 20%). We can predict that rocks with quantities of jarosite resulting in spectra with band depths of similar magnitude would be properly classified by this detector.

Band depth is a function of the combination of modal mineralogy, mineral composition and grain size; these factors are often unknown for planetary surfaces. We did not measure all of these characteristics for the samples used in this experiment, but we calculated modal estimates of jarosite abundance from the classification of backscatter electron (BSE) images. These estimates are rough, as the area displayed in a BSE image (∼tens of microns) is much smaller than then spot size of the VNIR spectrometer (centimeters) and these samples are typically heterogeneous over this range of scales. Jarosite abundance in 6 relatively homogeneous Sulfur Springs samples range from 19–49% (average = 28%) of the surface layers (∼the penetration depth of the spectrometer, ⩽20 microns). These samples were all correctly classified by the detector and have average BD (923) = 38% (range 26–56%) and BD (2267) = 17% (range 8–26%; Table 3). This is greater than, but comparable to the modeled jarosite abundance of 10% at the outcrops of Meridiani Planum (Clark et al., 2005). Thus there is at least one place on Mars where jarosite may occur in high enough abundance to be recognized by this detector.

At Sulfur Springs, jarosite is found in intimate mixtures of alunite (typically (K, Na)$Al_3(SO_4)_2(OH)_6$), goethite and gypsum ($CaSO_4{\cdot}2H_2O$), typically as rinds <5 microns thick upon alunite or layered within goethite (Greenwood et al., 2005,

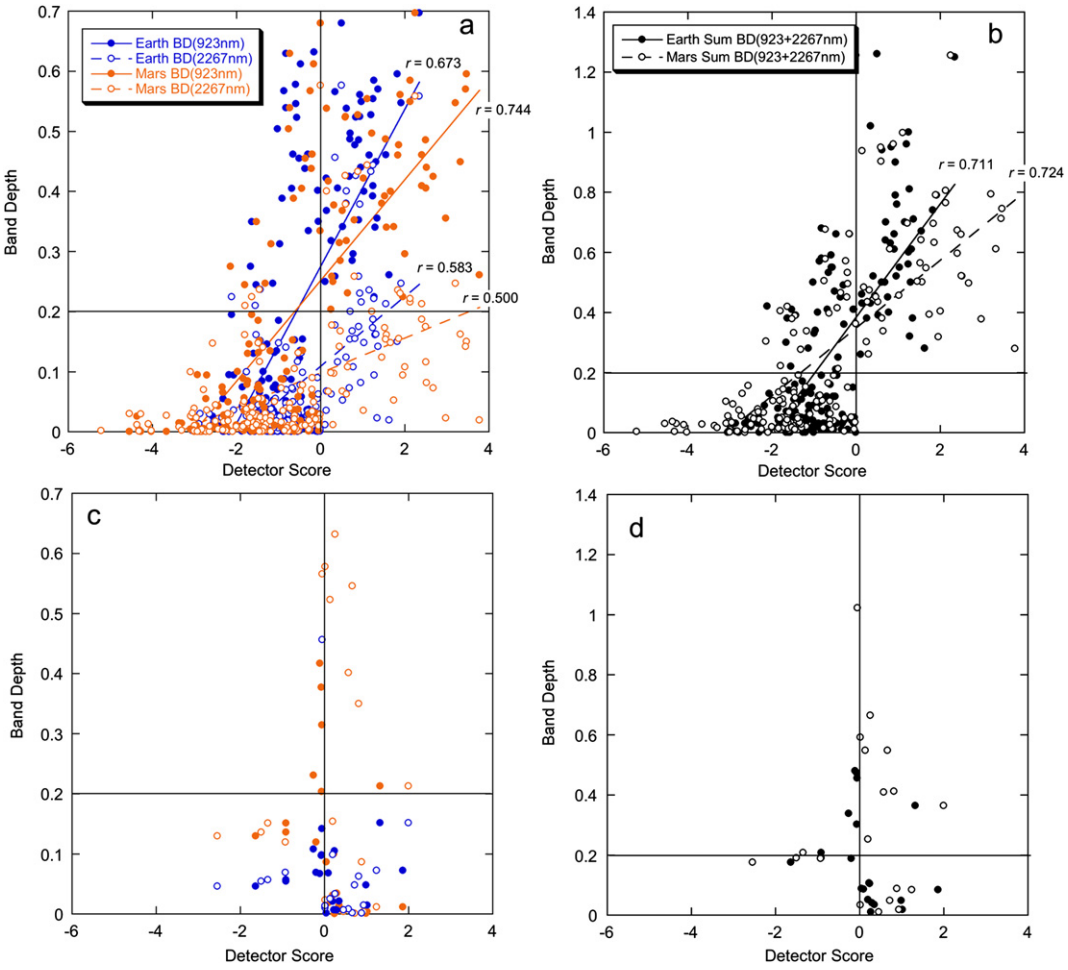

Fig. 6. Comparison of Earth- and Mars-optimized jarosite detector outputs to the band depths (BD) at 923 and 2267 nm of all spectra ($n = 185$). A detector output >0 is positive for jarosite. (a) A linear increase in detector output correlates with the strength of the primary jarosite absorptions as indicated by BD (923) and BD (2267) and their sum (b). Linear regressions are plotted. (c) Incorrect detections show no relationship between the detector score and BD (923), BD (2267) or their sum (d). The key for (a) is same as (c) and the key for (b) is the same as (d). The line at BD = 0.2 is for reference.

2006). Each of these minerals is recognizable in the spectra of the field samples. The detector is successful in distinguishing jarosite from these composite spectra of this hydrated assemblage of sulfates and iron hydroxide that is typical of acidic hydrothermal systems on Earth and likely Mars. The detector is also successful analyzing spectra collected under field conditions. We find that the detector performance is optimized by limiting the analysis to: (1) regions of the spectrum that are specific to jarosite and (2) the least noisy portions of the spectrum (avoidance of atmospheric contributions to the spectra). Other robust mineral detectors can be built using this architecture if they have absorption bands that are distinguishable from other common and associated minerals.

The algorithm is also able in most cases to distinguish jarosite from minerals that are spectrally similar within the detector input interval. Goethite, nontronite and hematite have primary absorptions at ~900 nm and nontronite has an additional absorption at ~2290 nm. That these minerals were properly distinguished from jarosite demonstrates the fact that the SVM incorporates spectral shape across the entire input range to classify each spectrum. Each of these minerals has been identified at Mars: hematite has been identified at both MER landing sites (Christensen et al., 2000; Klingelhöfer et al., 2004; Morris et al., 2006) and goethite has been identified in rocks in the Columbia Hills (Morris et al., 2006). The clay mineral nontronite has been identified on Mars by the OMEGA instrument on Mars Express (Poulet et al., 2005). Iron oxides and hydroxides may also occur with jarosite as a function of factors including pH, water/rock mass ratio, composition and fO_2 (Stoffregen et al., 2000; Zolotov and Shock, 2005). At Sulfur Springs, jarosite and goethite are found interlayered in several outcrops, where the jarosite layers are several microns thick. Hematite occurs with jarosite at the outcrops of the Opportunity landing site, where they may be genetically related (Klingelhöfer et al., 2004; McLennan et al., 2005). Thus it is important that the detector is able to distinguish jarosite from these associated and spectrally similar minerals.

Perhaps the greatest challenge to spectroscopy at the surface of Mars is the near-ubiquitous coating of fine-grained ferric dust. It is thus imperative that any mineral detector classify dust correctly and recognize target minerals within a spectrum containing dust. That the Earth-tuned detector misclassified two of the JSC Mars-1 samples is troubling, however the detector scores for these spectra were very close to the detector thresh-

Table 4
Jarosite detector performance

Experiment	Category	Earth atmosphere-tuned detector (% correct)	Mars atmosphere-tuned detector (% correct)
Museum quality samples (in lab)	Jarosite detection	8/8 (100)	7/8 (88)
	Non-jarosite rejection	24/26 (92)	24/26 (92)
Field samples (in lab)	Jarosite detection	16/21 (76)	17/21 (81)
	Non-jarosite rejection	54/59 (92)	54/59 (92)
Field-collected spectra	Jarosite detection	17/21 (81)	21/21 (100)
	Non-jarosite rejection	45/50 (90)	43/50 (86)
Overall performance		**164/185 (89%)**	**166/185 (90%)**

Table 5
Average values of band depth (BD) at 923 nm and 2267 nm and detector output of all samples ($n = 185$) for Earth (🌍) and Mars (👽)-tuned detectors

	True positives		True negatives		False positives		False negatives	
	🌍	👽	🌍	👽	🌍	👽	🌍	👽
N	41	45	123	121	12	14	9	5
BD (923)	44%	43%	11%	9%	4%	25%	21%	22%
BD (2267)	20%	19%	3%	3%	4%	4%	8%	14%
$\sum$BD	65%	61%	15%	12%	9%	29%	31%	36%
Detector score	0.96	1.59	−1.12	−1.72	0.58	0.62	−0.46	−1.27

old. These and other false positives could be reduced or eliminated for both detectors by increasing the detector output value that corresponds to a positive detection. For example, changing the detection threshold for both classifiers to 0.5 would reduce false positives by 67 and 47% while increasing false negatives by 17 and 18% for the Earth and Mars-tuned detectors, respectively. This conservative approach would minimize time allocation to the investigation of misidentified targets.

Although dust contaminates the majority of VNIR spectra, relatively dust-free rock surfaces have been identified at the Mars Pathfinder (Bell et al., 2000; Bridges et al., 2001) and Gusev crater sites (Farrand et al., 2006). Because VNIR point spectra are relatively computationally inexpensive to acquire, onboard processing of all spectra could potentially be accomplished to rapidly identify target minerals in the subset of dust-free or dust-poor rocks. At a rock or outcrop, rapid analysis of spectroscopic measurements could be used to identify targets for further measurement with more expensive mineralogical and geochemical analyses.

The detectors are computationally light and quickly process the reflectance data in our validation set. The input data are the ratio of radiance of the target and the radiance of a Lambertian reflector, where a dark current has been subtracted from both measurements. On board a rover, point spectra may not routinely be processed to reflectance using calibration targets. However, we predict that the detectors could run well on spectra that approximate reflectance, because the detectors are sensitive to the shape of mineral absorptions, not their absolute reflectance values. Conceivably, approximate reflectance could be calculated during standard rover operations by dividing each acquired point spectrum (or pixel converted to radiance in the case of an imager) by the solar radiance at the top of the martian atmosphere as has been done for Pancam (Bell et al., 2006). This product could be run through the detectors on board and returned or discarded as appropriate. The detectors could also be useful for the data mining of returned point spectra or multispectral or particularly hyperspectral imaging data, where all spectra and every pixel could be examined and prioritized by the classifiers.

The detectors described here also have the potential to strongly enhance the science return from hyperspectral imagers by performing onboard processing. Here again, data downlink restrictions highlight the need for robust mineral detection algorithms. Both OMEGA and CRISM will map only ~5% of the Mars surface at full spatial and spectral resolution during their nominal missions. While some targets are preselected for full resolution study (e.g., the MER landing sites), other high priority targets on Mars will be selected in response to observations made by the instruments in a multispectral survey mode. The jarosite detector and other mineral detection algorithms can be utilized to analyze any and all image cubes (x, y, λ) for a selected system. Such algorithms can help ensure that priority targets are not overlooked in these datasets.

Acknowledgments

This research is supported by the NASA Applied Information Systems Research Program. Thanks to C. Incarvito (XRD) and J. Eckert (SEM-EDS) at Yale University for analytical assistance. Field assistance by J. Andrew Gilmore is appreciated. Special thanks to the Sulfur Springs Park in St. Lucia managed by the Soufriere Foundation. Richard Maclin contributed to the development of the code used for the creation of the training data. Comments by Ed Cloutis and an anonymous reviewer are appreciated. In part, this work was carried out at the Jet Propulsion Laboratory, California Institute of Technology, under contract with the National Aeronautics and Space Administration.

References

Allen, C.C., Morris, R.V., Jagr, K.M., Golden, D.G., Lindstrom, D.J., Lindstrom, M.M., Lockwood, J.P., 1998. Martian regolith simulant JSC Mars-1. Lunar Planet. Sci. 29. Abstract 1690.

Bell III, J.F., Pollack, J.B., Geballe, T.R., Cruikshank, D.P., Freedman, R., 1994. Spectroscopy of Mars from 2.04 to 2.44 μm during the 1993 opposition: Absolute calibration and atmospheric vs mineralogic origin of narrow absorption features. Icarus 111, 106–123.

Bell III, J.F., McSween Jr., H.Y., Crisp, J.A., Morris, R.V., Murchie, S.L., Bridges, N.T., Johnson, J.R., Britt, D.T., Golombek, M.P., Moore, H.J., Ghosh, A., Bishop, J.L., Anderson, R.C., Brückner, J., Economou, T., Greenwood, J.P., Gunnlaugsson, H.P., Hargraves, R.M., Hviid, S., Knudsen, J.M., Madsen, M.B., Reid, R., Rieder, R., Soderblom, L., 2000. Mineralogic and compositional properties of martian soil and dust: Results from Mars Pathfinder. J. Geophys. Res. 105, 1721–1755.

Bell III, J.F., Squyres, S.W., Herkenhoff, K.E., Maki, J.N., Arneson, H.M., Brown, D., Collins, S.A., Dingizian, A., Elliot, S.T., Hagerott, E.C., Hayes,

A.G., Johnson, M.J., Johnson, J.R., Joseph, J., Kinch, K., Lemmon, M.T., Morris, R.V., Scherr, L., Schwochert, M., Shepard, M.K., Smith, G.H., Sohl-Dickstein, J.N., Sullivan, R.J., Sullivan, W.T., Wadsworth, M., 2003. Mars Exploration Rover Athena Panoramic Camera (Pancam) investigation. J. Geophys. Res. 108 (E12), doi:10.1029/2003JE002070. 8063.

Bell III, J.F., Squyres, S.W., Arvidson, R.E., Arneson, H.M., Bass, D., Calvin, W., Farrand, W.H., Goetz, W., Golombek, M., Greeley, R., Grotzinger, J., Guinness, E., Hayes, A.G., Hubbard, M.Y.H., Herkenhoff, K.E., Johnson, M.J., Johnson, J.R., Joseph, J., Kinch, K.M., Lemmon, M.T., Li, R., Mdsen, M.B., Maki, J.N., Malin, M., McCartney, E., McLennan, S., McSween Jr., H.Y., Ming, D.W., Morris, R.V., Noe Dobrea, E.Z., Parker, T.J., Proton, J., Rice, J.W. Jr., Seelos, F., Soderblom, J.M., Soderblom, L.A., Sohl-Dockstein, J.N., Sullivan, R.J., Weitz, C.M., Wolff, M.J., 2004. Pancam multispectral imaging results from the Opportunity rover at Merdiani Planum. Science 306, 1703–1709.

Bell III, J.F., Joseph, J., Sohl-Dickstein, J.N., Arneson, H.M., Johnson, M.J., Lemmon, M.T., Savransky, D., 2006. In-flight calibration and performance of the Mars Exploration Rovers Panoramic Camera (Pancam) instruments. J. Geophys. Res. 111, doi:10.1029/2005JE002444. E02S03.

Bibring, J.-P., Langevin, Y., Gendrin, A., Gondet, B., Poulet, F., Berthé, M., Soufflot, A., Arvidson, R., Mangold, N., Mustard, J., Drossart, P., the OMEGA team, 2005. Mars surface diversity as revealed by the OMEGA/Mars Express observations. Science 307, 1576–1581.

Bishop, J.L., Murad, E., 1996. Schwertmannite on Mars? Spectroscopic analyses of schwertmannite, its relationship to other ferric minerals, and its possible presence in the surface material on Mars. In: Dyar, M.D., McCannon, C., Schaefer, M.W. (Eds.), Mineral Spectroscopy: A Tribute to Roger G. Burns. Special Publication, No. 5. Geochemical Society, London, pp. 337–358.

Bishop, J.L., Murad, E., 2005. The visible and infrared spectral properties of jarosite and alunite. Am. Mineral. 90, 1100–1107.

Bishop, J.L., Madejová, J., Komadel, P., Fröschl, H., 2002. The influence of structural Fe, Al and Mg on the infrared OH bands in spectra of dioctahedral smectites. Clay Miner. 37, 607–616.

Bornstein, B., Castaño, R., Gilmore, M.S., Merrill, M., Greenwood, J.P., 2005. Creation and testing of an artificial neural network based carbonate detector for Mars rovers. In: Proceedings of the 2005 IEEE Aerospace Conference, Big Sky, MT, March 2005.

Bornstein, B., Fukunaga, A., Castaño, A., Biesiadecki, J., Castaño, R., Chien, S., Greeley, R., Whelley, P., Neakrase, L., Lemmon, M., 2007. Onboard science on the Mars Exploration Rovers: Cloud and dust devil detection. Lunar Planet. Sci. 38. Abstract 2339.

Bridges, N.T., Crisp, J.A., Bell III, J.F., 2001. Characteristics of the Pathfinder APXS sites: Implications for the composition of martian rocks and soils. J. Geophys. Res. 106, 14621–14665.

Calvin, W.M., King, T.V.V., Clark, R.N., 1994. Hydrous carbonates on Mars? Evidence from the Mariner 6/7 infrared spectrometer and groundbased telescopic spectra. J. Geophys. Res. 99, 14659–14675.

Castaño, A., Fukunaga, A., Biesiadecki, J., Castaño, R., Chien, S., 2006. Autonomous detection of dust devils and clouds in Mars. In: International Conference on Image Processing, Atlanta, GA, Oct. 2006.

Castaño, R., Estlin, T., Gaines, D., Castaño, A., Chouinard, C., Bornstein, B., Anderson, R.C., Chien, S., Fukunaga, A., Judd, M., 2006a. Opportunistic rover science. In: IEEE Aerospace Conference, Big Sky, MT, March 2006.

Castaño, R., Mazzoni, D., Tang, N., Greeley, R., Doggett, T., Cichy, B., Chien, S., Davies, A., 2006b. Onboard classifiers for Science Event Detection on a remote sensing spacecraft. In: ACM SIGKDD International Conference on Knowledge Discovery and Data Mining, Philadelphia, PA, August 2006.

Chien, S., Sherwood, R., Tran, S., Cichy, B., Rabideau, G., Castaño, R., Davies, A., Mandl, D., Frye, S., Trout, B., Shulman, S., Boyer, D., 2005. Using autonomy flight software to improve science return on Earth Observing One. J. Aerospace Comput. Inform. Commun. 2, 196–216.

Christensen, P.R., Bandfield, J.L., Clark, R.N., Edgett, K.S., Hamilton, V.E., Hoefen, T., Kieffer, H.H., Kuzmin, R.O., Lane, M.D., Malin, M.C., Morris, R.V., Pearl, J.C., Pearson, R., Roush, T.L., Ruff, S.W., Smith, M.D., 2000. Detection of crystalline hematite mineralization on Mars by the Thermal Emission Spectrometer: Evidence for near-surface water. J. Geophys. Res. 105, 9623–9642.

Clark, R.N., Roush, T.L., 1984. Reflectance spectroscopy: Quantitative analysis techniques for remote sensing applications. J. Geophys. Res. 89, 6329–6340.

Clark, R.N., King, T.V.V., Klejwa, M., Swayze, G., Vergo, N., 1990. High spectral resolution reflectance spectroscopy of minerals. J. Geophys. Res. 95, 12653–12680.

Clark, R.N., Swayze, G.A., Gallagher, A.J., King, T.V.V., Calvin, W.M., 1993. The US Geological Survey Digital Spectral Library Version 1: 0.2 to 3.0 microns. US Geological Survey Open File Report 93-592, http://speclab.cr.usgs.gov.

Clark, R.N., Swayze, G.A., Livo, K.E., Kokaly, R.F., Sutley, S.J., Dalton, J.B., McDougal, R.R., Gent, C.A., 2003. Imaging spectroscopy: Earth and planetary remote sensing with the USGS Tetracorder and expert systems. J. Geophys. Res. 108 (E12), doi:10.1029/2002JE001847. 5131.

Clark, B.C., Morris, R.V., McLennan, S.M., Gellert, R., Joliff, B., Knoll, A.H., Squyres, S.W., Lowenstein, T.K., Ming, D.W., Tosca, N.J., Yen, A., Christensen, P.R., Gorevan, S., Brückner, J., Calvin, W., Dreibus, G., Farrand, W., Klingelhöfer, G., Wänke, H., Zipfel, J., Bell III, J.F., Grotzinger, J., McSween, H.Y., Rieder, R., 2005. Chemistry and mineralogy of outcrops at Meridiani Planum. Earth Planet. Sci. Lett. 240, 73–94.

Cloutis, E.A., Hawthorne, F.C., Mertzman, S.A., Krenn, K., Craig, M.A., Marcino, D., Methot, M., Strong, J., Mustard, J.F., Blaney, D.L., Bell III, J.F., Vilas, F., 2006. Detection and discrimination of sulfate minerals using reflectance spectroscopy. Icarus 184, 121–157.

DeCoste, D., Mazzoni, D., 2003. Fast query-optimized kernel machine classification via incremental approximate nearest support vectors. In: International Conference on Machine Learning (ICML), August 2003.

Gaffey, S.J., 1987. Spectral reflectance of carbonate minerals in the visible and near-infrared (0.35–2.55 μm): Anhydrous carbonate minerals. J. Geophys. Res. 92, 1429–1440.

Gazis, P.R., Roush, T.L., 2001. Autonomous identification of carbonates using near-IR reflectance spectra during the February 1999 Marsokhod field tests. J. Geophys. Res. 106, 7765–7773.

Farrand, W.H., Bell III, J.F., Johnson, J.R., Squyres, S.W., Soderblom, J., Ming, D.W., 2006. Spectral variability among rocks in visible and near-infrared multispectral Pancam data collected at Gusev crater: Examinations using spectral mixture analysis and related techniques. J. Geophys. Res. 111, doi:10.1029/2005JE002495. E02S15.

Gilmore, M.S., Castaño, R., Mann, T., Anderson, R.C., Mjolsness, E.D., Manduchi, R., Saunders, R.S., 2000. Strategies for autonomous rovers at Mars. J. Geophys. Res. 105, 29223–29237.

Greenwood, J.P., Gilmore, M.S., Merrill, M.D., Blake, R.E., Martini, A.M., Varekamp, J.C., 2005. Jarosite mineralization on St. Lucia, WI: Preliminary geochemical, spectral and biological investigations of a martian analogue. Lunar Planet. Sci. 36. Abstract 2348 (CD-ROM).

Greenwood, J.P., Gilmore, M.S., Blake, R.E., Martini, A.M., Gomes, M., Tracy, S., Dyar, M.D., Gilmore, J.A., Varekamp, J.C., 2006. N ascent jarosite mineralization of Sulfur Springs, St. Lucia, WI: Implications for Meridiani jarosite formation. Lunar Planet. Sci. 37. Abstract 2230 (CD-ROM).

Hapke, B., 1993. Theory of Reflectance and Emittance Spectroscopy. Cambridge Univ. Press, New York.

Herr, K.C., Forney, P.B., Pimental, G.C., 1972. Mariner Mars 1969 infrared spectrometer. Appl. Opt. 11, 493–501.

Hunt, G.R., Ashley, R.P., 1979. Spectra of altered rocks in the visible and near infrared. Econ. Geol. 74, 1613–1628.

Hunt, G.R., Salisbury, J.W., 1970. Visible and near-infrared spectra of minerals and rocks. I. Silicate minerals. Mod. Geol. 1, 283–300.

Hunt, G.R., Salisbury, J.W., Lenhoff, C.J., 1971. Visible and near-infrared spectra of minerals and rocks. IV. Sulfides and sulfates. Mod. Geol. 3, 1–14.

Johnson, J.R., Ruff, S.W., Moersch, J., Roush, T., Horton, K., Bishop, J., Cabrol, N.A., Cockell, C., Gazis, P., Newsom, H.E., Stoker, C., 2001. Geological characterization of remote field sites using visible and infrared spectroscopy: Results from the 1999 Marsokhod field test. J. Geophys. Res. 106, 7683–7711.

Jolliff, B., Knoll, A., Morris, R.V., Moersch, J., McSween, H., Gilmore, M., Arvidson, R.E., Greeley, R., Herkenhoff, K., Squyres, S., 2002. Remotely sensed geology from lander-based to orbital perspectives: Results of FIDO rover May 2000 field tests. J. Geophys. Res. 107, doi:10.1029/2000JE001470.

Klingelhöfer, G., Morris, R.V., Bernhardt, B., Schröder, C., Rodionov, D.S., de Souza Jr., P.A., Yen, A., Gellert, R., Evlanov, E.N., Zubkov, B., Foh, J., Bonnes, U., Kankeleit, E., Gütlich, P., Ming, D.W., Renz, F., Wdowiak, T., Squyres, S.W., Arvidson, R.E., 2004. Jarosite and hematite at Meridiani Planum from Opportunity's Mössbauer Spectrometer. Science 306, 1740–1745.

Krenn, K.M., Cloutis, E.A., Russell, B., Kollar, S., Strong, J., 2001. Reflectance spectra of jarosite minerals: Implications for Mars. Lunar Planet. Sci. 32. Abstract 1223 (CD-ROM).

McLennan, S.M., Bell III, J.F., Calvin, W.M., Christensen, P.R., Clark, B.C., de Souza, P.A., Farmer, J., Farrand, W.H., Fike, D.A., Gellert, R., Ghosh, A., Glotch, T.D., Grotzinger, J.P., Hahn, B., Herkenhoff, K.E., Hurowitz, J.A., Johnson, J.R., Johnson, S.S., Joliff, B., Klingelhöfer, G., Knoll, A.H., Learner, Z., Malin, M.C., McSween Jr., H.Y., Pocock, J., Ruff, S.W., Soderblom, L.A., Squyres, S.W., Tosca, N.J., Watters, W.A., Wyatt, M.B., Yen, A., 2005. Provenance and diagenesis of the evaporite-bearing Burns formation, Meridiani Planum, Mars. Earth Planet. Sci. Lett. 240, 95–121.

Ming, D.W., Mittlefehldt, D.W., Morris, R.V., Golden, D.C., Gellert, R., Yen, A., Clark, B.C., Squyres, S.W., Farrand, W.H., Ruff, S.W., Arvidson, R.E., Klingelhöfer, G., McSween, H.Y., Rodionov, D.S., Schröder, C., de Souza Jr., P.A., Wang, A., 2006. Geochemical and mineralogical indicators for aqueous processes in the Columbia Hills of Gusev Crater, Mars. J. Geophys. Res. 111, doi:10.1029/2005JE002560.

Morris, R.V., Ming, D.W., Golden, D.C., Bell III, J.F., 1996. An occurrence of jarositic tephra on Mauna Kea, Hawaii: Implications for the ferric mineralogy of the martian surface. In: Dyar, M.D., McCammon, C., Shaefer, M.W. (Eds.), Mineral Spectroscopy: A Tribute to Roger G. Burns. Special Publication, No. 5. The Geochemical Society, London, pp. 327–336.

Morris, R.V., Klingelhöfer, G., Schröder, C., Rodionov, D.S., Yen, A., Ming, D.W., de Souza Jr., P.A., Fleischer, I., Wdowiak, T., Gellert, R., Bernhardt, B., Evlanov, E.N., Zubkov, B., Foh, J., Bonnes, U., Kankeleit, E., Gütlich, P., Renz, F., Squyres, S.W., Arvidson, R.A., 2006. Mössbauer mineralogy of rock, soil, and dust at Gusev crater, Mars: Spirit's journey through weakly altered olivine basalt on the Plains and pervasively altered basalt in the Columbia Hills. J. Geophys. Res. 111, doi:10.1029/2005JE002584. E02S13.

Mustard, J.F., Sunshine, J.M., 1995. Seeing through the dust: Martian crustal heterogeneity and links to the SNC meteorites. Science 267, 1623–1626.

Mustard, J.F., Erard, S., Bibring, J.-P., Head, J.W., Hurtrez, S., Langevin, Y., Pieters, C.M., Sotin, C.J., 1993. The surface of Syrtis Major: Composition of volcanic substrate and mixing with altered dust and soil. J. Geophys. Res. 98, 3387–3400.

Mustard, J.F., Murchie, S.L., Pelkey, S., Ehlmann, B.L., Milliken, R.E., Grant, J.A., Bibring, J.-P., Poulet, F., Bishop, J., Roach, L., Seelos, F., Humm, D., the CRISM Science Team, 2007. Overview of hydrated silicate minerals observed on Mars by CRISM. In: 7th International Conf. Mars. Abstract 3240.

Nesnas, I.A., Wright, A., Bajracharya, M., Simmons, R., Estlin, T., Kim, W.S., 2003. CLARAty: An Architecture for Reusable Robotic Software. In: SPIE Aerospace Conference, Orlando, FL, April 2003.

Owen, T., 1992. The composition and early history of the atmosphere of Mars. In: Kieffer, H.H., Jakosky, B.M., Snyder, C.W., Matthews, M.S. (Eds.), Mars. Univ. of Arizona Press, Tucson, pp. 818–834.

Poulet, F., Bibring, J.-P., Mustard, J.F., Gendrin, A., Mangold, N., Langevin, Y., Arvidson, R.E., Gondet, B., Gomez, C., the Omega Team, 2005. Phyllosilicates on Mars and implications for early martian climate. Nature 438, 623–627.

Ramsey, J., Gazis, P., Roush, T., Spirtes, P., Glymour, C., 2002. Automated remote sensing with near infrared reflectance spectra: Carbonate recognition. Data Mining Knowledge Discovery 6, 277–293.

Rossman, G.R., 1976. Spectroscopic and magnetic studies of ferric iron hydroxy sulfates: The series $Fe(OH)SO_4 \cdot nH_2O$ and the jarosites. Am. Mineral. 61, 398–404.

Schenker, P., 2006. Advances in rover technology for space exploration. In: IEEE Aerospace Conference, Big Sky, MT, March 2006.

Sherman, D.M., Vergo, N., 1988. Optical (diffuse reflectance) and Mössbauer spectroscopic study of nontronite and related Fe-bearing smectites. Am. Mineral. 73, 1346–1354.

Smith, P.H., Tomasko, M.G., Britt, D., Crowe, D.G., Reid, R., Keller, H.U., Thomas, N., Gliem, F., Rueffer, P., Sullivan, R., Greeley, R., Knudsen, J.M., Madsen, M.B., Gunnlaugsson, H.P., Hviid, S.F., Goetz, W., Soderblom, L.A., Gaddis, L., Kirk, R., 1997. The Imager for Mars Pathfinder experiment. J. Geophys. Res. 102, 4003–4025.

Stoffregen, R.E., Alpers, C.N., Jambor, J.L., 2000. Alunite–jarosite crystallography, thermodynamics, and geochronology. In: Alpers, C.N., Jambor, J.L., Nordstrom, D.K. (Eds.), Sulfate Minerals: Crystallography, Geochemistry and Environmental Significance. In: Reviews in Mineralogy and Geochemistry, vol. 40. Mineralogical Society of America, Washington, DC, pp. 453–479.

Wang, A., Korotev, R.L., Jolliff, B.L., Haskin, L.A., Crumpler, L., Farrand, W.H., Herkenhoff, K.E., de Souza Jr., P., Kusack, A.G., Hurowitz, J.A., Tosca, N.J., 2006. Evidence of phyllosilicates in Wooly Patch, an altered rock encountered at West Spur, Columbia Hills, by the Spirit rover in Gusev crater, Mars. J. Geophys. Res. 111, doi:10.1029/2005JE002516.

Zolotov, M.Y., Shock, E.L., 2005. Formation of jarosite-bearing deposits through aqueous oxidation of pyrite at Meridiani Planum, Mars. Geophys. Res. Lett. 32, doi:10.1029/2005GL024253. L21203.